Available online at www.sciencedirect.com

ScienceDirect

Journal of Sound and Vibration 304 (2007) 735–751

JOURNAL OF
SOUND AND
VIBRATION

www.elsevier.com/locate/jsvi

Spatial filtering and proper orthogonal decomposition of scanning laser Doppler vibrometry data for the nondestructive evaluation of frescoes

Richard J. Prazenica[a,*], Andrew J. Kurdila[b], Joseph F. Vignola[c]

[a] *University of Florida, Research and Engineering Education Facility, 1350 N. Poquito Rd., Shalimar, FL 32579-1163, USA*
[b] *Virginia Polytechnic Institute and State University, Department of Mechanical Engineering, 145 Durham Hall, Blacksburg, VA 24061, USA*
[c] *Department of Mechanical Engineering, The Catholic University of America, 620 Michigan Ave., N.E., Washington, DC 20064, USA*

Received 7 December 2005; received in revised form 26 February 2007; accepted 9 March 2007
Available online 7 May 2007

Abstract

Recently, scanning laser Doppler vibrometry experiments have been conducted in order to identify structural faults in frescoes at the US Capitol. In these experiments, the artwork is subjected to force excitations over a range of frequencies and a laser vibrometer is used to measure the velocity response of the structure over an array of spatial locations. At each frequency, a two-dimensional spatial image of the force–velocity transfer function is obtained. Spatial locations that consistently exhibit large responses are indicative of potential regions of delamination. In this paper the use of proper orthogonal decomposition, also known as principle component analysis, to identify coherent features in the structural response and obtain a succinct representation of the data is described. It is shown that, for the fresco studied in this paper, the response can be characterized in terms of only a few proper orthogonal decomposition modes. Unfortunately, these modes are corrupted by spatially varying noise. This noise is a result of surface irregularities that affect the direction in which the incident laser beam is reflected, which in turn corrupts the measured response at those locations. Therefore, the use of spatial filtering techniques is also explored for removing this "speckle noise" from the measured force–velocity transfer functions prior to performing the proper orthogonal decomposition analysis. Wavelets are particularly well suited for this application because they decompose images into functions that are localized in the spatial and frequency domains. In this paper, several wavelet bases with differing properties are used to filter the scanning laser Doppler vibrometry images. In addition, wavenumber filters, which essentially act as low-pass filters, are also employed. While the results do not definitively show which filtering technique is most effective for this application, it is clear that both wavelet processing and wavenumber filtering can reduce speckle noise while retaining the salient physical features in the image data. Therefore, it is demonstrated that proper orthogonal decomposition analysis coupled with spatial filtering is an effective tool for analyzing scanning laser Doppler vibrometry data in fault detection applications.

---

[*] Corresponding author. Tel.: +1 850 833 9350; fax: +1 850 833 9366.
E-mail address: prazenic@ufl.edu (R.J. Prazenica).

0022-460X/$ - see front matter © 2007 Elsevier Ltd. All rights reserved.
doi:10.1016/j.jsv.2007.03.027

1. Introduction

Over the past decade, numerous structural deficiencies have been observed and treated in frescoes at the US Capitol building. Frescoes are paintings that are built directly into walls or ceilings by applying paint to fresh plaster, examples of which include da Vinci's "Last Supper" painting and Michelangelo's ceiling of the Sistine Chapel. Over time, the structure of the plaster substrate that supports the artwork can become degraded, potentially leading to delamination or cracking of the fresco. In order to accurately assess the extent of structural plaster damage, the Physical Acoustics division of the US Naval Research Laboratory (NRL) began a broad survey ($\sim 700\,\mathrm{m}^2$) of the frescoes and wall paintings in the US Capitol Building in 2003. This study encompassed eight pre-selected spaces: Brumidi's first work at the Capitol building in the House Appropriations Committee room, the Parliamentarian's office, the House Speaker's office, the Senate Reception room, the President's Room, and three areas of the Brumidi Corridors [1].

In order to identify regions of potential degradation, the structure was excited by using either an electromechanical shaker or acoustical waves from a loudspeaker. A scanning laser Doppler vibrometer was used to measure the velocity response of the structure over a two-dimensional array of spatial locations and a range of excitation frequencies. Structural deficiencies are most likely to correspond to those locations that consistently exhibit high mobility. The scanning laser Doppler vibrometry technique, which was first applied to frescoes by researchers at the University of Ancona [2,3], mirrors the traditional "tap test" in which a curator taps at various locations on the artwork in order to audibly detect potential faults. In principle, the tap test is a qualitative measurement of the frequency changes that often signify a structural fault. Scanning laser Doppler vibrometry offers several obvious advantages over the tap test, namely that it is a relatively automated procedure and it does not require one to physically tap on the frescoes. Because it is a remote sensing technique, it does not require physical access to every test point. Therefore, for example, there is no need to erect a scaffolding to examine a painting on the ceiling. In scanning laser Doppler vibrometry experiments, the measured data consists of two-dimensional images that represent the force–velocity transfer function at each discrete excitation frequency. In the experiments conducted at the US Capitol, the size of the frescoes that were examined ranged from 1 to $4\,\mathrm{m}^2$, with a typical scan density of 400 points per square meter. At each spatial location, a linear chirp excitation was applied with a bandwidth ranging from under 100 Hz to 1 kHz.

In this paper, proper orthogonal decomposition (POD) is used to process the scanning laser Doppler vibrometry experimental data in an attempt to identify coherent features in the data. Proper orthogonal decomposition is a statistical method that uses covariance analysis to decompose the data into a series of modes through the solution of an eigenvalue problem. In many cases, such as in certain fluid flows, proper orthogonal decomposition has been used to generate reduced-order models of high-dimensional systems [4,5]. Indeed, as will be shown in this paper, proper orthogonal decomposition studies performed on scanning laser Doppler vibrometry data from the North Lunette fresco in the House Appropriations Committee Room have shown that only a few proper orthogonal decomposition modes are significant and the eigenvalue of the first proper orthogonal decomposition mode is an order of magnitude larger than the others. This result implies that, in this particular example, the most significant features in the data can be represented in terms of a single proper orthogonal decomposition mode. Unfortunately, when taking laser vibrometer measurements, surface irregularities can alter the direction in which the incident laser beam is reflected. Therefore, at certain locations the measured data is unreliable, resulting in a spatially varying "speckle noise". This speckle noise manifests itself in the proper orthogonal decomposition modes that are calculated from the raw scanning laser Doppler vibrometry data. Therefore, this paper investigates wavelet-based methods for filtering the scanning laser Doppler vibrometry images prior to performing proper orthogonal decomposition analysis. Wavelets and multiresolution analysis decompose image data in terms of functions that are localized in the spatial and frequency domains. In this paper, several wavelet bases are employed including the Haar basis, biorthogonal wavelets, and piecewise-polynomial orthonormal multiwavelets. Alternatively, wavenumber filters, which effectively act as spatial low-pass filters, are used to remove small-scale features (i.e., speckle noise) in the data. Proper orthogonal decomposition results obtained from the wavenumber filtered data and the wavelet-processed data are compared with those generated from the raw data, demonstrating the benefits of filtering prior to applying the proper orthogonal decomposition analysis.

2. Scanning laser Doppler vibrometry experimentation

The scanning laser Doppler vibrometry apparatus consists of two parts: an excitation mechanism and a measurement system. A schematic of the setup is shown in Fig. 1. Excitation may be accomplished either acoustically or electromechanically. In the acoustical method, a multifrequency chirp is repeatedly directed at the artwork by a set of loudspeakers operating at approximately ~90 dB. Because they have greater mobility, areas with defects respond with greater displacement and velocity amplitudes than typical "intact" regions of the wall. The scanning laser Doppler vibrometry instrument is used to measure the velocity response, allowing precise identification of regions suspected of defect in the structure. In the mechanical method, the artwork is excited by an electromechanical shaker rather than a sound wave. This is done by means of a shaker with a Teflon-coated tip that leans against the fresco and propagates the multifrequency chirp directly into the wall, without the intervening medium of air. This method is analogous to the conservator's "tap test", and has some advantages over the loudspeaker method. For example, it transfers energy more efficiently into the artwork and is less disruptive to the surrounding workplace.

Velocity data is collected by a Polytec scanning laser Doppler vibrometry which uses a laser emitting ~1 mW of power at a wavelength of 6328 A. Such a low level of laser power does no harm to the artwork and may be used around humans without any special safety precautions. Velocities are derived from the measured Doppler shifts of light rays reflected off the vibrating surface. Once the velocity data has been collected, it undergoes a suite of post-processing. The result is a color-coded overlay which may be superimposed on an image of the artwork to give a precise map of the location of structural defects. By "defects" this paper refers to all manner of cracks, delaminations, detachments, and inhomogeneities. For more information on the scanning laser Doppler vibrometry technique, see Refs. [2,3,6].

A scanning laser Doppler vibrometry scan file contains data that may be interpreted as a complex-valued function on a three-dimensional space. The first two dimensions are simply the spatial coordinates, labeled m and n. The third coordinate is frequency, labeled k. The amplitude of the complex-valued function corresponds to velocity at that particular location in three-space. Explicitly, the scanning laser Doppler vibrometry assigns to each point in $\{m, n, k\}$-space a velocity amplitude $X_{(m,n),k}$. The subscript $(m,n), k$ emphasizes that the velocity is associated with physical grid point (m,n) and excitation frequency k. Fig. 2 is an illustration of the array of raw experimental data being collected.

For example, a graphical display of scanning laser Doppler vibrometry data taken from the North Lunette Fresco in the Speakers Appropriations Committee Room of the Capitol, shown in Fig. 3, is given in Fig. 4.

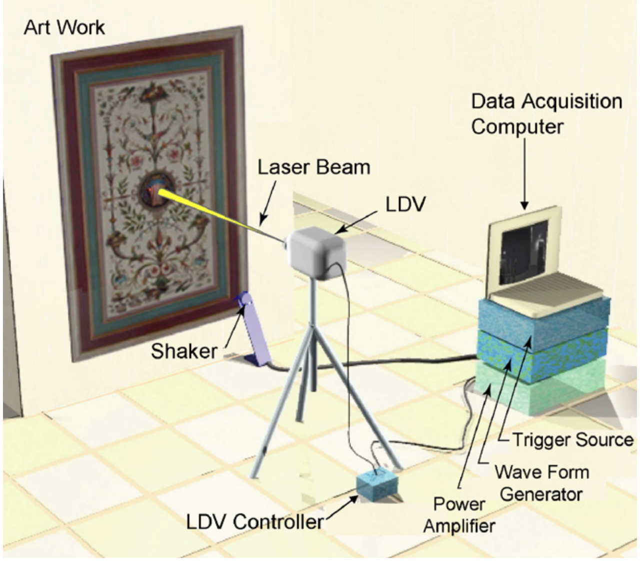

Fig. 1. Schematic of scanning laser Doppler vibrometry experiment for nondestructive evaluation of frescoes.

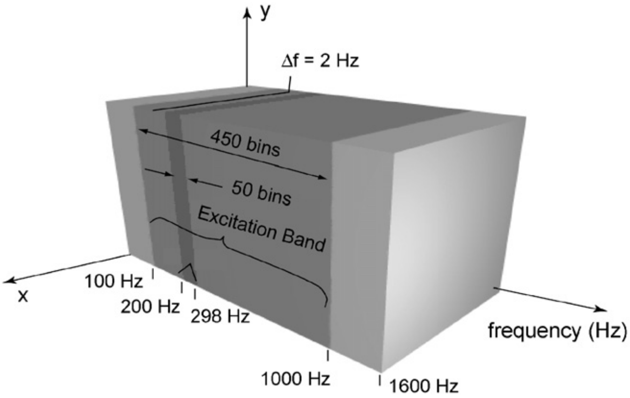

Fig. 2. Graphical depiction of the three-dimensional scanning laser Doppler vibrometry data array. The elements of the data array are complex-valued, force-normalized velocities for a given spatial location and frequency.

Fig. 3. North Lunette Fresco, House Appropriations Committee Room.

Each thumbnail image in Fig. 4 displays the characteristic response within the specified frequency bin of each point scanned on the artwork. By visually comparing different thumbnails (i.e., responses at different frequencies) points can be identified where the velocity response is persistently high across a range of frequencies. These are points of unusually high mobility; they correspond to points where the substructure may have been compromised.

3. Proper orthogonal decomposition

Several analytical tools have been used in this survey to analyze the data acquired in the scanning laser Doppler vibrometry experiments. In this paper, proper orthogonal decomposition, a common approach for post-processing time series, is used to extract the essential features from the scanning laser Doppler vibrometry data. This method is also known in statistical applications as principal component analysis, or covariance analysis, of the time series. Depending on the context, proper orthogonal decomposition/principal component

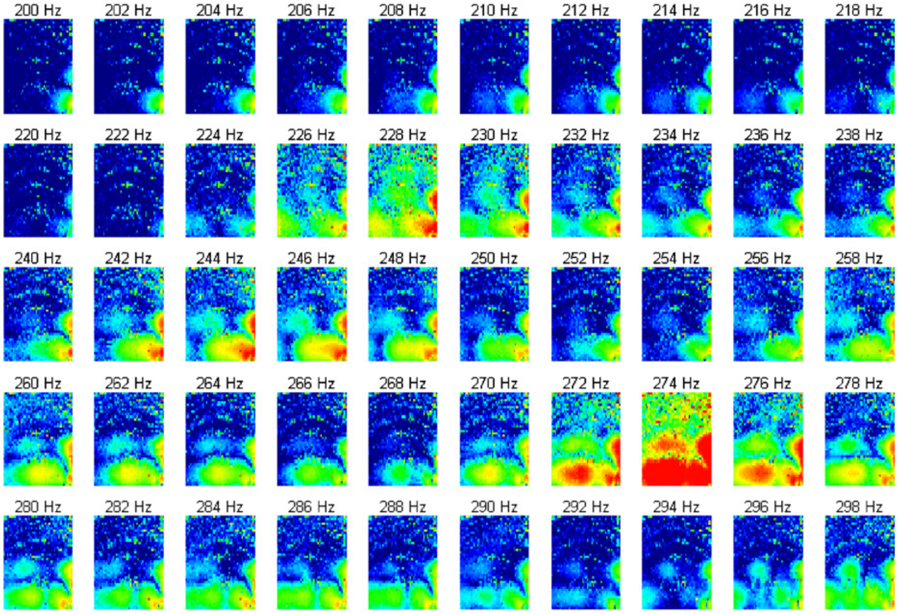

Fig. 4. Magnitude of force–velocity transfer functions over the X–Y scan region for a frequency range of 200–298 Hz.

analysis methods are described as methods that extract the coherent structures in a vector field or extract the statistically most significant components of a time series [7]. In this paper, the proper orthogonal decomposition method is generalized for a multidimensional (two spatial, one spectral) analysis of the vibratory response. An operator-theoretic description of the foundations of proper orthogonal decomposition can be found in many sources including Lumley [4], who first used the proper orthogonal decomposition method to describe large eddy coherent structures in a turbulent boundary layer, and Holmes [5]. Alternatively, descriptions based on statistical notions may be found in Ref. [8]. The description that follows is statistical in nature. This context is chosen because the theoretical discussion is more concise in this case.

Suppose that $\{\mathbf{X}_k : 1 \leqslant k \leqslant n_F\}$ represents some stochastic process. The index k may be thought of as referring to "frames of data". Each of the frames of data might be comprised of several channels of simultaneous measurements. In the application discussed in this paper, the set $\{\mathbf{X}_k : 1 \leqslant k \leqslant n_F\}$ is the collection of scanned velocity data indexed by the frequency bin, where n_F is the total number of frequency bins. Each of the random variables $\mathbf{X}_k$ is assumed to be an $n_X \times 1$ column vector whose individual components are scalar random variables $X_{j,k}$, where $1 \leqslant j \leqslant n_X$ and $1 \leqslant k \leqslant n_F$. If the stochastic process $\{\mathbf{X}_k : 1 \leqslant k \leqslant n_F\}$ has zero mean, the covariance matrix is given by

$$\mathbf{C} = \frac{1}{n_F} \sum_{k=1}^{n_F} \mathbf{X}_k \mathbf{X}_k^{\mathrm{T}}, \tag{1}$$

with individual entries

$$C_{i,j} = \frac{1}{n_F} \sum_{k=1}^{n_F} X_{i,k} X_{j,k}. \tag{2}$$

Otherwise, the covariance matrix is given by

$$\mathbf{C} = \frac{1}{n_F} \sum_{k=1}^{n_F} (\mathbf{X}_k - E(\mathbf{X}))(\mathbf{X}_k - E(\mathbf{X}))^{\mathrm{T}}. \tag{3}$$

In this expression, $E(\mathbf{X})$ is the expected value of the stochastic process $\{\mathbf{X}_k : 1 \leqslant k \leqslant n_F\}$ and hence it is an $n_X \times 1$ column vector.

It only remains to carry out the modicum of book-keeping required to map the two-dimensional arrays obtained from the scanning laser Doppler vibrometry scans, which are indexed by frequency bin, to the framework outlined above. Each frequency bin $k \in \{1, \ldots, n_F\}$ can be viewed as a two-dimensional array $\mathbf{A}_k$ whose entries are denoted $A_{(m,n),k}$, where m is the row index and n is the column index in the array. It is assumed that $1 \leqslant m \leqslant n_R$ and $1 \leqslant n \leqslant n_C$, where n_R and n_C are the number of rows and columns, respectively, in the two-dimensional array. In this case, these two indices will correspond to a two-dimensional spatial location in a two-dimensional grid. By unpacking the two-dimensional arrays $\{\mathbf{A}_k : 1 \leqslant k \leqslant n_F\}$ (in either row major or column major format), it is straightforward to define the vector of random variables $\mathbf{X}_k$. Introduce the correspondences

$$\begin{aligned} X_{j,k} &\Leftrightarrow A_{(m,n),k} \\ j &\Leftrightarrow (m,n) \end{aligned} \tag{4}$$

and define $n_X = n_R n_C$. The entries of the covariance matrix defined in Eq. (3) then take the form

$$C_{(m,n),(s,t)} = \frac{1}{n_F} \sum_{k=1}^{n_F} (A_{(m,n),k} - E(A_{(m,n)}))(A_{(s,t),k} - E(A_{(s,t)})), \tag{5}$$

where $E(A_{(m,n)})$ represents the expected value of $\{A_{(m,n),k} : 1 \leqslant k \leqslant n_F\}$.

Once the covariance matrix has been computed, coherent patterns appearing in the collection of two-dimensional arrays $\{\mathbf{A}_k : 1 \leqslant k \leqslant n_F\}$ can be determined directly. The $n_X \times n_X$ eigenvalue problem

$$\{\mathbf{C} - \lambda_k \mathbf{I}\}\Psi_k = 0 \tag{6}$$

must be solved for n_X eigenvalues and eigenvectors $\{(\lambda_k, \Psi_k) | k = 1, \ldots, n_X\}$. Again, each eigenvector will have length n_X and there will be n_X real eigenvalues since the covariance matrix is real and symmetric. A physical interpretation of the one-dimensional eigenvectors $\{\Psi_k\}$ is achieved by renumbering their entries into matrices $\{\Phi_k\}$ in exactly the same fashion that the two-dimensional arrays $\{\mathbf{A}_k\}$ are associated with one-dimensional vectors $\{\mathbf{X}_k\}$. That is, define the correspondences

$$\begin{aligned} \Psi_{j,k} &\Leftrightarrow \Phi_{(m,n),k} \\ j &\Leftrightarrow (m,n). \end{aligned} \tag{7}$$

Images of coherent structures are obtained by ordering the eigenvectors according to the magnitude of the corresponding eigenvalues. The contribution of a particular eigenvector-image to the subspace spanned by all n_F frames of data can be rigorously related to the magnitude of the corresponding eigenvalue. Thus, for some integer n_K of kept modes that satisfies $n_K \leqslant n_X$ and $n_K \leqslant n_F$, the images

$$\{\Phi_k \,|\, k = 1, \ldots, n_K\} \subset \{\Phi_k \,|\, k = 1, \ldots, n_X\} \tag{8}$$

are retained as a good representation of the coherent features in the original data set.

4. Wavelets and multiresolution analysis

Spatially varying speckle noise in the raw scanning laser Doppler vibrometry data scans can contribute to spurious proper orthogonal decomposition modes. In this paper, wavelets and multiresolution analysis are used to filter the scanning laser Doppler vibrometry data scans prior to applying the proper orthogonal decomposition algorithm. Generally speaking, wavelets are compactly supported, oscillatory functions designed to satisfy certain properties such as orthogonality or biorthogonality, smoothness, and symmetry or antisymmetry. A wavelet basis is obtained from the scaled translates and dilates of a small number of wavelet functions. The resulting basis is composed of wavelet functions that are localized in both the spatial and wavenumber domains. Therefore, a wavelet decomposition (or wavelet transform) yields information regarding the spatial location of wavenumber components occurring within a signal. For this reason, wavelets and multiresolution analysis have been widely applied for the filtering of signals and images. The multiresolution-based structure of the wavelet transform is effective for differentiating coherent features in the image from noise artifacts. The wavelet coefficients corresponding to the noise are then removed, effectively replacing the noisy data with spatially averaged data from adjacent locations.

Numerous wavelet families with differing combinations of properties have been constructed for a myriad of applications. Therefore, there are many options for the image processing application discussed in this paper and it is difficult, if not impossible, to determine *a priori* which choice of wavelet basis will yield the best results. In this paper, three wavelet bases are considered for filtering scanning laser Doppler vibrometry data. These include the well-known Haar basis, a biorthogonal wavelet basis, and a piecewise-polynomial, orthonormal multiwavelet basis. Each has certain advantages and disadvantages that are representative of the trade-offs one typically encounters when choosing a wavelet basis for a particular application. Before delving into the differences between these three wavelet families, this section provides a review of the basic principles of wavelet representations of functions and, in particular, two-dimensional images. While well known in the image processing community (see, for example, Refs. [9,10]), this overview is provided for readers less familiar with this family of spatial analysis techniques. The discussion is given in the general context of biorthogonal multiwavelets, of which each of the specific wavelet bases considered in this paper is a special case.

A multiwavelet basis for $L^2(\mathbb{R})$, the space of square-integrable functions, is composed of the scaled translates and dilates of multiple wavelet functions $\{\psi^1, \ldots, \psi^r\}$ that are generated from r scaling functions $\{\phi^1, \ldots, \phi^r\}$. In biorthogonal multiwavelet families, there exists a set of dual scaling functions $\{\tilde{\phi}^1, \ldots, \tilde{\phi}^r\}$ that generate a set of dual wavelets $\{\tilde{\psi}^1, \ldots, \tilde{\psi}^r\}$ such that the following biorthogonality relationships are satisfied, $\forall k, m \in \mathbb{Z}$, and $s, t \in \{1, \ldots, r\}$:

$$\begin{aligned}
&\int_{\mathbb{R}} \phi^s(x-k)\tilde{\phi}^t(x-m)\,\mathrm{d}x = \delta_{s,t}\delta_{k,m}\\
&\int_{\mathbb{R}} \psi^s(x-k)\tilde{\psi}^t(x-m)\,\mathrm{d}x = \delta_{s,t}\delta_{k,m}\\
&\int_{\mathbb{R}} \psi^s(x-k)\tilde{\phi}^t(x-m)\,\mathrm{d}x = 0\\
&\int_{\mathbb{R}} \phi^s(x-k)\tilde{\psi}^t(x-m)\,\mathrm{d}x = 0
\end{aligned} \tag{9}$$

where $\mathbb{Z}$ is the set of all integers and the Kronecker delta $\delta_{s,t}$ is defined in the usual manner as

$$\delta_{s,t} = \begin{cases} 1 & s = t, \\ 0 & s \neq t. \end{cases} \tag{10}$$

The scaling functions $\{\phi^1, \ldots, \phi^r\}$ and wavelets $\{\psi^1, \ldots, \psi^r\}$ are commonly termed the analysis scaling functions and wavelets while their dual counterparts are often termed the synthesis scaling functions and wavelets. Here, it should be noted that a large number of wavelet families can be considered special cases of biorthogonal multiwavelets. The vast majority of biorthogonal wavelet families in the literature correspond to the single generator case where there is a single scaling function and wavelet pair (ϕ, ψ) and an associated dual pair $(\tilde{\phi}, \tilde{\psi})$. Orthonormal wavelets are self-dual; that is, the dual scaling functions and wavelets are equivalent to the original analysis scaling functions and wavelets. Once again, the single generator case constitutes by far the largest number of orthonormal wavelet families. For the purposes of this paper, then, biorthogonal multiwavelets represent the most general class of wavelet bases.

By construction, the analysis scaling functions and wavelets and their dual counterparts satisfy the two-scale relationships:

$$\begin{aligned}
\phi^s(x) &= \sqrt{2}\sum_{p,t} a_p^{s,t}\phi^t(2x-p), & \tilde{\phi}^s(x) &= \sqrt{2}\sum_{q,t} \tilde{a}_q^{s,t}\tilde{\phi}^t(2x-q),\\
\psi^s(x) &= \sqrt{2}\sum_{p,t} b_p^{s,t}\phi^t(2x-p), & \tilde{\psi}^s(x) &= \sqrt{2}\sum_{q,t} \tilde{b}_q^{s,t}\tilde{\phi}^t(2x-q),
\end{aligned} \tag{11}$$

for $s = 1, \ldots, r$. The two-scale equations state that the scaling functions and wavelets are formed as linear combinations of scaling functions with half the support (or double the frequency). The analysis scaling functions and wavelets are ultimately defined by the filters $\{a_p^{s,t}\}$ and $\{b_p^{s,t}\}$. Similarly, the dual scaling functions and wavelets are uniquely defined via the filters $\{\tilde{a}_p^{s,t}\}$ and $\{\tilde{b}_p^{s,t}\}$. The scaled translates and dilates of these functions are defined using the notation

$$\begin{aligned}\phi_{j,k}^s(x) = 2^{j/2}\phi^s(2^j x - k), \quad \tilde{\phi}_{j,k}^s(x) = 2^{j/2}\tilde{\phi}^s(2^j x - k),\\ \psi_{j,k}^s(x) = 2^{j/2}\psi^s(2^j x - k), \quad \tilde{\psi}_{j,k}^s(x) = 2^{j/2}\tilde{\psi}^s(2^j x - k).\end{aligned} \tag{12}$$

The parameter $j \in \mathbb{Z}$ is a dilation index that defines the scale, or resolution level, of the function. The parameter $k \in \mathbb{Z}$ is a translation index that determines the position of the function on the real line. The $2^{j/2}$ term is a normalization factor that renders the functions orthonormal in $L^2(\mathbb{R})$.

The scaled translates and dilates of the scaling functions are the generators of a series of approximation spaces $\{V_j\}_{j\in\mathbb{Z}}$, where each space V_j is defined as

$$V_j = \mathrm{span}\{\phi_{j,k}^s : s \in \{1,\ldots,r\},\ k \in \mathbb{Z}\}. \tag{13}$$

The spaces $\{V_j\}$ are nested such that

$$\{0\} \subset \cdots \subset V_{j-1} \subset V_j \subset V_{j+1} \subset \cdots L^2(\mathbb{R}). \tag{14}$$

This series of approximation spaces is termed a multiresolution analysis because it enables one to view a function or signal at varying levels of resolution. In a similar manner, the scaled translates and dilates of the wavelets form a series of spaces $\{W_j\}_{j\in\mathbb{Z}}$, where each space W_j is defined as

$$W_j = \mathrm{span}\{\psi_{j,k}^s : s \in \{1,\ldots,r\},\ k \in \mathbb{Z}\}. \tag{15}$$

Each wavelet space W_j represents the difference between two adjacent approximation spaces such that

$$V_j = V_{j-1} \oplus W_{j-1}, \tag{16}$$

where $\oplus$ denotes the addition of vector spaces. In other words, the space W_j provides the details that are present in the approximation of a function in V_j but do not appear in the coarser approximation in V_{j-1}. Given that each approximation space can be decomposed in this manner, a recursive application of Eq. (16) yields the following decomposition of V_j:

$$V_j = V_{j_0} \oplus W_{j_0} \oplus W_{j_0-1} \oplus \cdots \oplus W_{j-2} \oplus W_{j-1}, \tag{17}$$

where j_0 is the coarsest resolution level in the decomposition. In the limit as $j \to \infty$ and $j_0 \to -\infty$,

$$L^2(\mathbb{R}) = \sum_{l=-\infty}^{\infty} W_l. \tag{18}$$

That is, the scaled translates and dilates of the wavelets $\{\psi^1,\ldots,\psi^r\}$ form a basis for $L^2(\mathbb{R})$. It should be noted that, in an analogous manner, a multiresolution analysis $\{\tilde{V}_j\}_{j\in\mathbb{Z}}$ is generated by the dual scaling functions $\{\tilde{\phi}^1,\ldots,\tilde{\phi}^r\}$ and a series of wavelet spaces $\{\tilde{W}_j\}_{j\in\mathbb{Z}}$ is formed from the dual wavelets $\{\tilde{\psi}^1,\ldots,\tilde{\psi}^r\}$.

A multiwavelet-based representation of a one-dimensional function f is obtained by first forming a single-scale expansion of the function in V_j:

$$f_j(x) = \sum_{k\in\mathbb{Z}}\sum_{s=1}^{r} \alpha_{j,k}^s \phi_{j,k}^s(x). \tag{19}$$

By using the biorthogonality of the scaling functions, the single-scale coefficients $\{\alpha_{j,k}^s\}$ can be computed as

$$\alpha_{j,p}^s = \int_{\mathbb{R}} f(x)\tilde{\phi}_{j,p}^s(x)\,\mathrm{d}x. \tag{20}$$

In many cases, especially when the scaling functions are not defined in closed form, the single-scale coefficients are taken as sampled values of the function f. Such an approximation is reasonable if the resolution level j is sufficiently fine. Eq. (17) implies that an equivalent multiscale representation of f_j can be written as

$$f_j(x) = \sum_{k\in\mathbb{Z}}\sum_{s=1}^{r} \alpha_{j_0,k}^s \phi_{j_0,k}^s(x) + \sum_{l=j_0}^{j-1}\sum_{k\in\mathbb{Z}}\sum_{s=1}^{r} \beta_{l,k}^s \psi_{l,k}^s(x). \tag{21}$$

This multiscale representation is in terms of wavelets on resolution levels j_0 through $j-1$ and scaling functions on the coarsest level j_0. In this representation, the contribution of the scaling functions on the coarsest resolution level can be viewed as a low-pass filtering of the function f while the wavelets on different resolution levels act as a series of band-pass filters. The attractiveness of the multiscale representation in Eq. (21) is that it provides information in both the spatial and frequency domains.

A key property of biorthogonal multiwavelets is that the multiscale basis coefficients can be calculated from the single-scale coefficients in Eq. (19) in a fast, efficient manner. This is accomplished by using the decomposition formulas

$$\alpha^s_{j-1,m} = \sum_k \sum_{t=1}^{r} \tilde{a}^{s,t}_{k-2m} \alpha^t_{j,k}, \tag{22}$$

$$\beta^s_{j-1,m} = \sum_k \sum_{t=1}^{r} \tilde{b}^{s,t}_{k-2m} \alpha^t_{j,k}. \tag{23}$$

These formulas are derived by using the two-scale equations and the biorthogonality properties of the scaling functions and wavelets. Note, in particular, that the *dual* scaling function and wavelet filters $\{\tilde{a}^{s,t}_p\}$ and $\{\tilde{b}^{s,t}_p\}$ appear in these decomposition formulas. Eqs. (22) and (23) can be used to compute the decomposition of scaling coefficients on one resolution level into scaling and wavelet coefficients on the next coarser level, as in Eq. (16). Applied recursively to the scaling coefficients at each level, these formulas are used to compute the set of multiscale coefficients in Eq. (21). Similarly, the single-scale coefficients can be reconstructed from the multiscale coefficients through a recursive application of the reconstruction formula

$$\alpha^s_{j,m} = \sum_{t=1}^{r} \sum_k a^{t,s}_{m-2k} \alpha^t_{j-1,k} + \sum_{t=1}^{r} \sum_k b^{t,s}_{m-2k} \beta^t_{j-1,k}. \tag{24}$$

Note that the analysis scaling function and wavelet filters $\{a^{s,t}_p\}$ and $\{b^{s,t}_p\}$ are used in the reconstruction.

Most importantly for the image filtering application discussed in this paper, the representation of two-dimensional functions or images is achieved by using two-dimensional scaling functions and wavelets that are formed from the tensor products of the one-dimensional functions. Thus, we obtain the following sets of analysis and dual two-dimensional scaling functions and wavelets:

$$\begin{aligned}
\Phi^{(s,t)}(x,y) &= \phi^s(x)\phi^t(y), & \tilde{\Phi}^{(s,t)}(x,y) &= \tilde{\phi}^s(x)\tilde{\phi}^t(y),\\
\Psi^{1,(s,t)}(x,y) &= \phi^s(x)\psi^t(y), & \tilde{\Psi}^{1,(s,t)}(x,y) &= \tilde{\phi}^s(x)\tilde{\psi}^t(y),\\
\Psi^{2,(s,t)}(x,y) &= \psi^s(x)\phi^t(y), & \tilde{\Psi}^{2,(s,t)}(x,y) &= \tilde{\psi}^s(x)\tilde{\phi}^t(y),\\
\Psi^{3,(s,t)}(x,y) &= \psi^s(x)\psi^t(y), & \tilde{\Psi}^{3,(s,t)}(x,y) &= \tilde{\psi}^s(x)\tilde{\psi}^t(y),
\end{aligned} \tag{25}$$

where $s, t \in \{1, \ldots, r\}$. We introduce the following notation for the scaled translates and dilates of the two-dimensional functions:

$$\begin{aligned}
\Phi^{(s,t)}_{j,(k,m)}(x,y) &= \phi^s_{j,k}(x)\phi^t_{j,m}(y), & \tilde{\Phi}^{(s,t)}_{j,(k,m)}(x,y) &= \tilde{\phi}^s_{j,k}(x)\tilde{\phi}^t_{j,m}(y),\\
\Psi^{1,(s,t)}_{j,(k,m)}(x,y) &= \phi^s_{j,k}(x)\psi^t_{j,m}(y), & \tilde{\Psi}^{1,(s,t)}_{j,(k,m)}(x,y) &= \tilde{\phi}^s_{j,k}(x)\tilde{\psi}^t_{j,m}(y),\\
\Psi^{2,(s,t)}_{j,(k,m)}(x,y) &= \psi^s_{j,k}(x)\phi^t_{j,m}(y), & \tilde{\Psi}^{2,(s,t)}_{j,(k,m)}(x,y) &= \tilde{\psi}^s_{j,k}(x)\tilde{\phi}^t_{j,m}(y),\\
\Psi^{3,(s,t)}_{j,(k,m)}(x,y) &= \psi^s_{j,k}(x)\psi^t_{j,m}(y), & \tilde{\Psi}^{3,(s,t)}_{j,(k,m)}(x,y) &= \tilde{\psi}^s_{j,k}(x)\tilde{\psi}^t_{j,m}(y).
\end{aligned} \tag{26}$$

Similar to the one-dimensional case, the scaling functions are the generators of a multiresolution analysis $\{V_j\}_{j\in\mathbb{Z}}$ where

$$V_j = \operatorname{span}\{\Phi^{(s,t)}_{j,(k,m)} : s, t \in \{1, \ldots, r\},\ k, m \in \mathbb{Z}\}. \tag{27}$$

The wavelet spaces are defined as

$$W^p_j = \operatorname{span}\{\Psi^{p,(s,t)}_{j,(k,m)} : s, t \in \{1, \ldots, r\},\ k, m \in \mathbb{Z}\}, \quad p = 1, 2, 3, \tag{28}$$

such that the space V_j can be decomposed as

$$V_j = V_{j-1} \oplus W^1_{j-1} \oplus W^2_{j-1} \oplus W^3_{j-1}. \tag{29}$$

Over multiple resolution levels, we have

$$V_j = V_{j_0} \bigoplus_{l=j_0}^{j-1} \{W^1_l \oplus W^2_l \oplus W^3_l\}, \tag{30}$$

where, once again, j_0 is the coarsest resolution level in the decomposition.

A single-scale representation of a two-dimensional function f, such as an image, can be written as

$$f_j(x,y) = \sum_{k,m\in\mathbb{Z}} \sum_{s,t=1}^{r} \alpha^{(s,t)}_{j,(k,m)} \Phi^{(s,t)}_{j,(k,m)}(x,y). \tag{31}$$

An equivalent, multiscale expansion is given by

$$\begin{aligned} f_j(x,y) = {} & \sum_{k,m\in\mathbb{Z}} \sum_{s,t=1}^{r} \alpha^{(s,t)}_{j_0,(k,m)} \Phi^{(s,t)}_{j_0,(k,m)}(x,y) \\ & + \sum_{l=j_0}^{j-1} \sum_{k,m\in\mathbb{Z}} \sum_{s,t=1}^{r} \beta^{1,(s,t)}_{l,(k,m)} \Psi^{1,(s,t)}_{l,(k,m)}(x,y) \\ & + \sum_{l=j_0}^{j-1} \sum_{k,m\in\mathbb{Z}} \sum_{s,t=1}^{r} \beta^{2,(s,t)}_{l,(k,m)} \Psi^{2,(s,t)}_{l,(k,m)}(x,y) \\ & + \sum_{l=j_0}^{j-1} \sum_{k,m\in\mathbb{Z}} \sum_{s,t=1}^{r} \beta^{3,(s,t)}_{l,(k,m)} \Psi^{3,(s,t)}_{l,(k,m)}(x,y). \end{aligned} \tag{32}$$

In decomposing an image, the scaling functions on the coarsest level produce a large-scale averaging, or low-pass filtering, of the image while the wavelets provide details at different resolution levels. The three different types of wavelets each focus on a particular form of detail in the image. The type 1 wavelets provide the most detail about horizontal features, the type 2 wavelets focus the most on vertical features, and the type 3 wavelets are best-suited for extracting diagonal details. As in the one-dimensional case, the multiscale basis coefficients in Eq. (32) can be computed from the single-scale coefficients in Eq. (31) via a recursive application of the decomposition formulas

$$\begin{aligned} \alpha^{(u,v)}_{j-1,(a,c)} &= \sum_{k,m,s,t} \tilde{a}^{u,s}_{k-2a} \tilde{a}^{v,t}_{m-2c} \alpha^{(s,t)}_{j,(k,m)}, \\ \beta^{1,(u,v)}_{j-1,(a,c)} &= \sum_{k,m,s,t} \tilde{a}^{u,s}_{k-2a} \tilde{b}^{v,t}_{m-2c} \alpha^{(s,t)}_{j,(k,m)}, \\ \beta^{2,(u,v)}_{j-1,(a,c)} &= \sum_{k,m,s,t} \tilde{b}^{u,s}_{k-2a} \tilde{a}^{v,t}_{m-2c} \alpha^{(s,t)}_{j,(k,m)}, \\ \beta^{3,(u,v)}_{j-1,(a,c)} &= \sum_{k,m,s,t} \tilde{b}^{u,s}_{k-2a} \tilde{b}^{v,t}_{m-2c} \alpha^{(s,t)}_{j,(k,m)}. \end{aligned} \tag{33}$$

The single-scale coefficients can be recovered from the multiscale coefficients by using the reconstruction formula

$$\begin{aligned} \alpha^{(u,v)}_{j,(a,c)} = \sum_{k,m,s,t} \{ & a^{s,u}_{a-2k} a^{t,v}_{c-2m} \alpha^{(s,t)}_{j-1,(k,m)} + a^{s,u}_{a-2k} b^{t,v}_{c-2m} \beta^{1,(s,t)}_{j-1,(k,m)} \\ & + b^{s,u}_{a-2k} a^{t,v}_{c-2m} \beta^{2,(s,t)}_{j-1,(k,m)} + b^{s,u}_{a-2k} b^{t,v}_{c-2m} \beta^{3,(s,t)}_{j-1,(k,m)} \}. \end{aligned} \tag{34}$$

5. Wavelet-based image processing

The preceding section has provided the necessary background for the application of wavelets to the filtering of images. In this section, the wavelet-based filtering procedure using three different wavelet bases with varying properties is discussed. In addition, an alternative approach, that of using wavenumber filters, which are essentially spatial low-pass filters, is presented for comparison with the wavelet-based techniques.

5.1. Wavelet-based filtering

Regardless of the particular wavelet basis employed within the broad classification of biorthogonal multiwavelets, one obtains a multiscale representation of the original image I that takes the general form in Eq. (32). This representation is obtained by first computing a single-scale approximation of the image, which requires the calculation of the basis coefficients in Eq. (31). The original image is represented in terms of pixels and thus can be viewed as a two-dimensional, piecewise-constant function of the form

$$I(x,y) = \sum_{p=1}^{n_x} \sum_{q=1}^{n_y} c_{j,(p,q)} \chi_{j,(p,q)}(x,y). \tag{35}$$

where $\chi_{j,(p,q)}$ is the characteristic function over one pixel, defined as

$$\chi_{j,(p,q)}(x,y) = \begin{cases} 1 & x \in [2^{-j}p, 2^{-j}(p+1)] \text{ and } y \in [2^{-j}q, 2^{-j}(q+1)], \\ 0 & \text{otherwise}, \end{cases} \tag{36}$$

and $j, p, q \in \mathbb{Z}$. The coefficients $\{c_{j,(p,q)}\}$ are then simply equivalent to the grayscale pixel values. In Eq. (35), n_x denotes the number of horizontal pixels while n_y is the number of vertical pixels. Note that, for ease of computation with wavelets, it has been assumed that the pixel size is dyadic (i.e. a power of two). While this may not be the case for the original image, the representation in Eq. (35) can be obtained via an appropriate rescaling of the image. The single-scale basis coefficients can be obtained by computing directly, via integration, the projection of the original image representation in Eq. (35) onto the scaling functions in Eq. (31). Then, a multiscale representation of the image can be generated in a fast, efficient manner by using the decomposition formulas given in Eq. (33) to compute the multiscale basis coefficients.

The multiscale representation of the image given by Eq. (32) contains all of the information present in the original image. Thus, any noise in the original image is also contained in the wavelet representation. The standard approach to denoising is to remove those wavelet coefficients whose absolute values are below a given threshold T [9]. Removing these small coefficients amounts to the elimination of low-amplitude noisy variations in the image. Denoting the entire set of multiscale coefficients generically as $\{\beta_k\}$, a hard thresholding strategy can be used to compute a new set of coefficients $\{\hat{\beta}_k\}$ as

$$\hat{\beta}_k = \begin{cases} \beta_k & |\beta_k| > T, \\ 0 & |\beta_k| \leqslant T. \end{cases} \tag{37}$$

Alternatively, a soft thresholding strategy can be employed:

$$\hat{\beta}_k = \begin{cases} \beta_k - T & \beta_k > T, \\ \beta_k + T & \beta_k < -T, \\ 0 & |\beta_k| \leqslant T. \end{cases} \tag{38}$$

The soft thresholding approach provides additional smoothing of the original image. Donoho [10] showed that the estimation error associated with thresholding can be guaranteed to be no more than a $2\ln(N)$ factor larger than the ideal estimation error (i.e., the wavelet estimation error if it were possible to perfectly extract the image from the noise) provided that the threshold value is chosen to be

$$T = \sigma\sqrt{2\ln(N)}, \tag{39}$$

where N is the total number of basis coefficients and σ is the standard deviation of the noise. For Gaussian white noise, Donoho [10] showed that σ can be estimated in terms of the median of the finest-scale wavelet coefficients, which we denote as $\{\beta_{j-1,k}\}$:

$$\hat{\sigma} = \frac{1}{0.6745}\mathrm{Med}(\{\beta_{j-1,k}\}). \tag{40}$$

A more detailed discussion can be found in the signal processing text by Mallat [9].

While the above denoising approach is optimal for images corrupted by Gaussian white noise, it is not optimal for the scanning laser Doppler vibrometry images studied in this paper. The laser vibrometry data is subject to a spatially varying noise that is a result of variations in the texture of the object being measured (i.e., a fresco). These textural variations result in the incident laser beam not being directly reflected back to the vibrometer. Thus, as the laser vibrometer scans an area, certain locations do not yield reliable data, resulting in speckle noise. The speckle noise typically appears on the smallest scale (on the order of one pixel) and a reasonable approach would be to remove the corrupted pixels and replace them with averages of surrounding pixels. To do this perfectly would require a great deal of user interaction in processing each image. Clearly, an automated approach is desired since the proper orthogonal decomposition analysis incorporates many image frames.

One approach to eliminating speckle noise is to apply a spatial low-pass filter to the raw image data. The implicit assumption here is that the useful information, the regions of high mobility that are indicative of delamination, is present over large scales (or low wavenumbers) while the speckle noise occurs at high spatial wavenumbers. The wavenumber filtering approach essentially denoises the images by performing this type of low-pass filtering. Wavenumber domain analysis reveals a broad range of elastic wave speeds present in the structures, some as low as ~30 m/s. Wave speeds are derived from two-dimensional spatial Fourier transforms of the decomposed scanning laser Doppler vibrometry data. Because the multiscale wavelet representations of images are equivalent to a low-pass filter and a series of band-pass filters acting on the image, wavelets can also be used to perform spatial low-pass filtering. This is accomplished by truncating the vector of multiscale wavelet coefficients, retaining only those coefficients on the coarser resolution levels. Eliminating entire levels of resolution is arguably the simplest wavelet-based filtering strategy but may also correspond to the most effective means for eliminating speckle noise. The approach taken is this paper is to both truncate the coefficients on the finest resolution levels and apply soft thresholding to the remaining coefficients.

5.2. *Wavelet bases*

In this paper the performance of three different wavelet bases for the filtering of scanning laser Doppler vibrometry image data are considered. Each of these bases can be considered a special case in the general class of biorthogonal multiwavelets.

5.2.1. *Haar wavelet*

The Haar wavelet is the simplest wavelet and is typically used as a prototype for studying more complicated wavelet families (see, for example, Refs. [9,10]). The Haar family consists of a single orthonormal scaling function and wavelet pair (ϕ, ψ). Thus, it is a special case of self-dual, single-generator biorthogonal multiwavelets. The advantage of working with the Haar basis is that it is composed of piecewise-constant functions, capable of exactly representing images, which can be viewed as piecewise-constant surfaces whose amplitudes correspond to the pixel intensity values. In addition, the Haar basis is supported over square domains with no overlap, so there is no need for any special boundary treatments. The final advantage of the Haar basis is the ease of computation: there are only two filter coefficients and the simple form of the functions renders them easy to plot. The main disadvantage of the Haar basis is that, because the functions are piecewise-constant, they do not yield smooth representations. This may not seem like a disadvantage when working with images that have discrete pixels, but some smoothness is desirable once the filtering has been performed.

5.2.2. *Cohen, Daubechies and Feaveau biorthogonal wavelets*

The second wavelet basis considered in this paper is a single-generator family of biorthogonal wavelets constructed by Cohen et al. [11]. The particular choice of the analysis scaling function and wavelet pair (ϕ, ψ) is much smoother than the Haar scaling function and wavelet. The dual scaling function and wavelet pair $(\tilde{\phi}, \tilde{\psi})$, not explicitly used in the image approximation, is actually equivalent to the Haar scaling function and wavelet. The main advantage of these biorthogonal wavelets over the Haar basis is the increased smoothness of the image approximation. One disadvantage of this biorthogonal basis is that the functions must be adapted to the finite boundaries of the image. This requires some form of boundary extension (e.g., symmetric, antisymmetric, or periodic) that inevitably introduces error in the form of edge artifacts in the image representation. The analysis scaling functions are also not available in closed form, making it more difficult to compute the coefficients of the single-scale representation via integration. Instead, the single-scale coefficients are approximated as scaled samples of the image (i.e., pixel values). Such an approximation is reasonable if the resolution level is sufficiently fine.

5.2.3. *Donovan, Geronimo and Hardin piecewise-linear multiwavelets*

The final wavelet basis employed in this paper is a piecewise-polynomial family of orthonormal multiwavelets. In particular, a set of piecewise-linear scaling functions and associated wavelets, constructed by Donovan et al. [12] via the technique of intertwining, is used. These functions are orthonormal and can be adapted to the finite image domain in a straightforward manner. Because the functions are piecewise-linear in form, it is relatively easy to perform quadratures to compute the single-scale basis coefficients. It should be noted that piecewise-quadratic and piecewise-cubic multiwavelets have also been constructed using the same techniques, but these bases were not considered in this paper. The main disadvantage of using these multiwavelets is the additional computational burden associated with using multiple scaling functions and wavelets. Due to computational considerations, there is a limit on the finest resolution level that can be used for the single-scale representation of the image. Thus, in this case, some *a priori* smoothing of the image takes place before performing the wavelet transform and filtering.

5.3. *Filtering example*

Wavenumber filters and the three different wavelet bases have been used to filter the raw scanning laser Doppler vibrometry images. As an example, the magnitude of the original force–velocity transfer function for the North Lunette fresco at a frequency of 246 Hz and the filtered images obtained by using the three wavelet bases and two wavenumber filters are shown in Fig. 5. The first wavenumber filter corresponds to a mild low-pass filter while the second wavenumber filter performs a strong low-pass filtering of the image. In all cases, the images have been plotted on a dB scale. Each of the filtered images, to a certain degree, exhibits less of the speckle noise evident in the original image. The difference between the mild and strong wavenumber filters is clear, with the strong filter providing a more aggressive denoising of the image. The piecewise-linear multiwavelets appear to perform better than the Haar and biorthogonal wavelets. In particular, some edge effects are evident in the image that was filtered using biorthogonal wavelets.

6. Experimental results

The filtered scanning laser Doppler vibrometry data have been processed using proper orthogonal decomposition analysis. In this example, there were a total of 251 discrete frequencies, corresponding to a bandwidth of 100–600 Hz in increments of 2 Hz. The first 5 proper orthogonal decomposition modes obtained by using the raw scanning laser Doppler vibrometry image data without the benefit of filtering are shown in Fig. 6. Also shown is a plot of the first 10 eigenvalues from which it is evident that the first eigenvalue is a full order of magnitude larger than the next largest eigenvalue. Therefore, the vast majority of energy resides in the first proper orthogonal decomposition mode and the other modes are relatively insignificant. The first proper orthogonal decomposition mode shows large areas of potential delamination both at the bottom of the fresco and on the lower right side. Note that a significant amount of speckle noise appears in each of these modes. It is interesting to note that proper orthogonal decomposition possesses some inherent denoising properties in

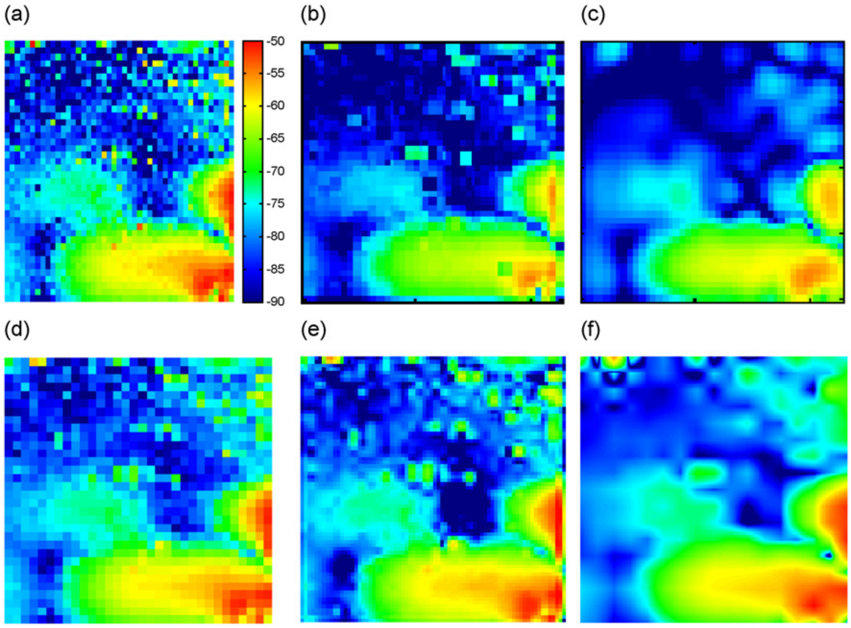

Fig. 5. Filtering of the force-transfer function at 246 Hz using wavenumber filtering and wavelets: (a) original image; (b) mild wavenumber filtering; (c) strong wavenumber filtering; (d) Haar wavelet filtering; (e) biorthogonal wavelet filtering; (f) multiwavelet filtering.

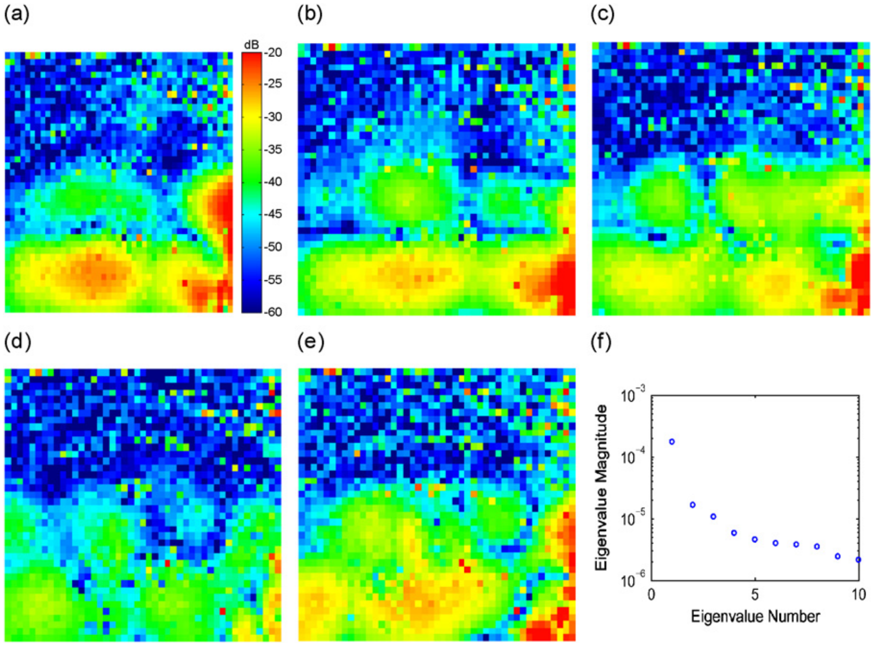

Fig. 6. First 5 proper orthogonal decomposition modes using raw image data without filtering: (a) first mode; (b) second mode; (c) third mode; (d) fourth mode; (e) fifth mode; (f) eigenvalues.

that the noise typically appears in the less significant modes associated with the smaller eigenvalues. This would be the case for a Gaussian white noise distribution, for example. Speckle noise is unique, however, in that it is caused by surface irregularities on the artwork; therefore, the noise appears in the same spatial locations in the force–velocity transfer function images independent of frequency. As a result, speckle noise is

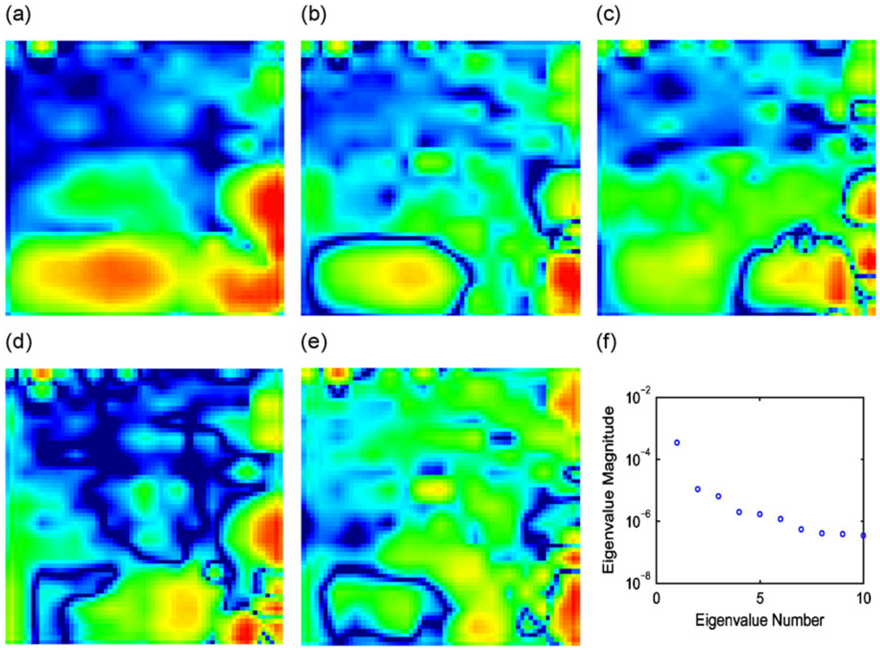

Fig. 7. First 5 proper orthogonal decomposition modes obtained from images that have been filtered using piecewise-linear multiwavelets: (a) first mode; (b) second mode; (c) third mode; (d) fourth mode; (e) fifth mode; (f) eigenvalues.

a highly coherent feature in the transfer function images and appears in the most significant proper orthogonal decomposition modes.

Fig. 7 illustrates the first 5 proper orthogonal decomposition modes generated from the multiwavelet-processed data. The first mode clearly resembles the one generated from the raw data but contains less noise. It is interesting to note that the other modes in Fig. 7 do not resemble those in Fig. 6. Once again, these modes are not very significant, as evidenced by the relative size of the first eigenvalue. Noise in the scanning laser Doppler vibrometry data can result in spurious proper orthogonal decomposition modes, which may explain the vast differences between the proper orthogonal decomposition modes from the raw data and the denoised data. In Fig. 8 are shown the first proper orthogonal decomposition mode obtained from the raw data, the wavenumber filtered data, and the wavelet-processed data. In all cases, the wavenumber filtering and wavelet-based filtering results in a reduction of speckle noise in the first proper orthogonal decomposition mode. While the results are qualitatively similar, all three wavelet-based approaches retain some features in the upper left and right-hand corners of the image that have been removed by both wavenumber filters. Whether these features are noise artifacts that the wavelets failed to remove or true physical features that the wavenumber filters failed to retain is an open issue that requires further investigation. Therefore, this study does not clearly demonstrate the relative superiority of either the wavenumber filtering or the wavelet-based filtering approach. It is clear, however, that either of these filtering methods, when applied to the raw scanning laser Doppler vibrometry image data prior to performing proper orthogonal decomposition analysis, results in a cleaner, more accurate set of proper orthogonal decomposition modes.

7. Conclusion

In this paper, the analysis of scanning laser Doppler vibrometry data for fault detection in frescoes at the US Capitol has been described. During these experiments, several paintings were subjected to force excitations, in the form of mechanical or acoustical inputs, over a range of frequencies. A scanning laser Doppler vibrometer was used to measure the velocity response of the artwork over an array of spatial locations. Qualitatively, spatial locations that consistently exhibit large velocity responses correspond to areas

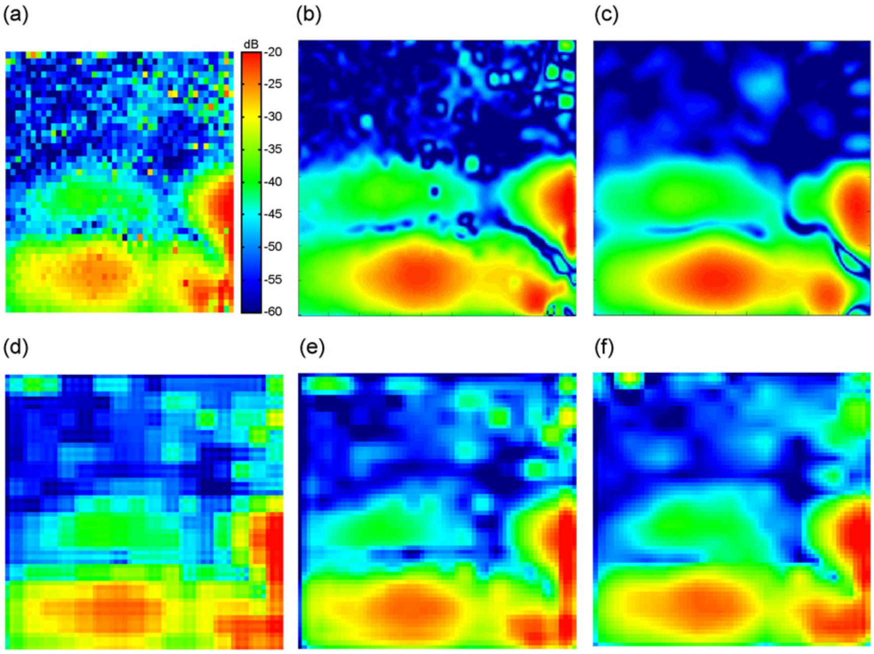

Fig. 8. Comparison of the first proper orthogonal decomposition mode obtained from the raw image data, weak and strong wavenumber filtering, and wavelet filtering: (a) raw image data; (b) weak wavenumber filtering; (c) strong wavenumber filtering; (d) Haar wavelet filtering; (e) biorthogonal wavelet filtering; (f) multiwavelet filtering.

of possible structural degradation. The experimental data is obtained in the form of a three-dimensional force–velocity transfer function that can be viewed as a series of two-dimensional spatial images. Each of these images represents the transfer function within a discrete frequency bin.

The use of proper orthogonal decomposition has been explored as a means of efficiently analyzing this large quantity of experimental data. Proper orthogonal decomposition is a covariance-based statistical method that decomposes the data into a series of orthogonal modes. These modes are given as the eigenvectors generated by solving an eigenvalue problem, where the magnitude of each eigenvalue is proportional to the energy contained in the corresponding mode. In this paper, scanning laser Doppler vibrometry data taken from the North Lunette fresco in the House Appropriations Room was analyzed using proper orthogonal decomposition. In this example, the frequency ranged from 100 to 600 Hz in increments of 2 Hz, for a total of 251 images. The proper orthogonal decomposition analysis showed that the data could be represented in terms of 5 modes, where the first eigenvalue was an order of magnitude larger than the next largest one. Therefore, in this case, it was shown that a single proper orthogonal decomposition mode was actually sufficient to capture the salient features in the scanning laser Doppler vibrometry data.

While proper orthogonal decomposition can provide efficient representations of large quantities of scanning laser Doppler vibrometry data, the individual images are corrupted with spatially varying speckle noise due to irregularities on the surface of the artwork. It is interesting to note that proper orthogonal decomposition analysis generally provides some denoising by associating the noise with the smaller, less significant eigenvalues. In this application, however, the spatial dependence of the noise results in high coherence across the transfer function images at different frequencies. Therefore, speckle noise appears in the most significant proper orthogonal decomposition modes and can also result in the identification of spurious modes. As such, another important goal of this paper has been to explore spatial filtering methods for removing speckle noise from the images prior to performing proper orthogonal decomposition analysis. The Haar wavelet basis, biorthogonal wavelets, and piecewise-linear orthonormal multiwavelets were all employed for image filtering with the best qualitative performance provided by the multiwavelets. Both mild and strong wavenumber filters were also used to filter the data. In all cases, when proper orthogonal decomposition analysis was performed using the filtered scanning laser Doppler vibrometry data, a cleaner set of proper orthogonal decomposition modes was obtained. While the wavenumber filters and wavelet-based methods both reduced the amount of noise in the dominant proper orthogonal decomposition mode, the wavelet-based techniques retained some features that were removed by the wavenumber filters. Further investigation is required in order to determine if these retained features have any physical significance or if they are merely noise artifacts. Therefore, the limited study described in this paper does not clearly demonstrate which filtering approach, the wavenumber filtering or the wavelet-based processing, is most effective for this application. The results do clearly show, however, that proper orthogonal decomposition analysis coupled with image filtering provides a potentially powerful tool for the evaluation of scanning laser Doppler vibrometry data for fault detection.

Acknowledgments

The authors would like to thank the anonymous reviewers and the editors for their thoughtful comments and suggestions for improving this manuscript.

References

[1] B.A. Wolanin, *Constantino Brumidi*: *Artist of the Capitol*, US Government Printing Office, Washington, DC, 1998.
[2] P. Castellini, N. Paone, E.P. Tomasini, Application of a laser Doppler vibrometer to nonintrusive diagnostic of frescoes damage, *Proceedings of the SPIE* 2358 (1994) 70–77.
[3] P. Castellini, N. Paone, E.P. Tomasini, The laser Doppler vibrometer as an instrument for nonintrusive diagnostic of works of art: application to fresco paintings, *Optics and Lasers in Engineering* 25 (1996) 227–246.
[4] J.L. Lumley, Coherent structures in turbulence, in: R.E. Meyer (Ed.), *Transition and Turbulence*, Academic Press, New York, 1981, pp. 215–242.
[5] P. Holmes, J.L. Lumley, G. Berkooz, *Turbulence, Coherent Structures, Dynamical Systems and Symmetry*, Cambridge University Press, Cambridge, 1996.
[6] C.B. Scruby, L.E. Drain, *Laser Ultrasonics: Techniques and Applications*, Adam Hilger, Bristol, England, 1990.
[7] G. Kerschen, J.-C. Golinval, A.F. Vakakis, L.A. Bergman, The method of proper orthogonal decomposition for dynamical characterization and order reduction of mechanical systems: an overview, *Nonlinear Dynamics* 41 (2005) 147–169.
[8] A.V. Oppenheim, R.W. Schafer, *Digital Signal Processing*, Prentice-Hall, Englewood Cliffs, NJ, 1975.
[9] S. Mallat, *A Wavelet Tour of Signal Processing*, Academic Press, New York, 1998.
[10] D. Donoho, I. Johnstone, Ideal spatial adaptation via wavelet shrinkage, *Biometrika* 81 (1994) 425–455.
[11] A. Cohen, I. Daubechies, J.C. Feauveau, Biorthogonal bases of compactly supported wavelets, *Communications on Pure and Applied Mathematics* 45 (1992) 485–559.
[12] G. Donovan, J. Geronimo, D. Hardin, Intertwining multiresolution analyses and the construction of piecewise-polynomial wavelets, *SIAM Journal of Mathematical Analysis* 27 (6) (1996) 1791–1815.